Scilight

Dynamic Nanocatalysis

https://www.sciltp.com/journals/dn

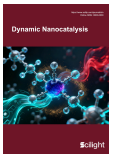

Review

Check for updates

Modification Strategies of WO_3-Based Photoanodes for Enhanced Photoelectrochemical Water Splitting

Lu Zhang [1], Mengnan Ruan [1,2], Chengyi Wang [1,2], Li Zhou [1,2] and Zhifeng Liu [1,2,*]

[1] School of Materials Science and Engineering, Tianjin Chengjian University, Tianjin 300384, China
[2] Tianjin Key Laboratory of Building Green Functional Materials, Tianjin Chengjian University, Tianjin 300384, China
* Correspondence: tjulzf@163.com

How To Cite: Zhang, L.; Ruan, M.; Wang, C.; et al. Modification Strategies of WO_3-Based Photoanodes for Enhanced Photoelectrochemical Water Splitting. *Dynamic Nanocatalysis* **2026**, *1*(1), 2. https://doi.org/10.53941/dn.2026.100002

Received: 22 March 2026
Revised: 21 April 2026
Accepted: 22 April 2026
Published: 30 April 2026

Abstract: Photoelectrochemical (PEC) water splitting, a core technology for converting solar energy to hydrogen, has evolved into a promising approach to mitigate global energy depletion and environmental pollution. As one of the most important photoanodes, WO_3 possesses prominent photostability and an appropriately aligned energy band structure. However, its efficiency in PEC water splitting is limited by issues such as the sluggish surface OER reaction kinetics, the limited light absorption range and the recombination of photogenerated carriers. In this review, a thorough overview of promising strategies for WO_3-based photoanodes was presented, including morphology control, doping, OER cocatalysts modification, heterostructure construction and surface plasmon resonance (SPR)-enhanced surface modification strategy. Furthermore, we outlined the prospect and outlook of WO_3-based photoanodes, along with the corresponding optimization strategies, relevant computational research progress and practical applicability evaluation, aiming to provide meaningful guidance for the rational design and large-scale application of WO_3-based photoelectrodes.

Keywords: WO_3; photoanodes; photoelectrochemical water splitting; modification strategies

1. Introduction

The rapid development of human society, coupled with the excessive depletion of conventional energy resources, has led to energy shortages and environmental degradation, which has emerged as a critical impediment to the sustainable progress of human civilization [1–3]. Therefore, constructing a clean and environmentally sustainable renewable energy system has become a critical strategy for global researchers to address this issue [4]. Hydrogen, characterized by its high calorific value and carbon-neutral combustion products, has been identified as an ideal renewable energy carrier [5–7].

Nevertheless, fossil fuels remain dominant in global hydrogen production, serving as merely a temporary fix for current issues [8]. It is inconsistent with the long-term goals of carbon neutrality and environmental protection [9]. Consequently, hydrogen production via renewable energy conversion pathways has attracted extensive research endeavors. As an unbounded, plentiful, widely distributed and sustainable resource, solar energy is a primary choice among diverse renewable energy sources for hydrogen production [10]. In 1972, Fujishima and Honda made a groundbreaking discovery that TiO_2 was capable of producing hydrogen through PEC water dissociation, achieving the solar-to-hydrogen energy conversion [11]. This discovery stimulated great enthusiasm for the high-performance photoelectrode materials for PEC systems. With the continuous research, more semiconductor materials for PEC have been discovered. Typical examples of n-type semiconductors applied as the photoanodes include ZnO [12], WO_3 [13], Fe_2O_3 [14], $SrTiO_3$ [15], $BaTiO_3$ [16], etc., while p-type semiconductors employed as the photocathodes involve CdS [17], Cu_2O [18], InP [19], Si [20], GaP [21] among others.

In practice, PEC systems for hydrogen production have not yet been widely commercialized, which is attributed to the limited light absorption range of the catalyst, slow surface reaction kinetics, and severe recombination of photogenerated carriers [22]. To solve these problems, researchers have conducted extensive studies on different catalyst systems. Transition metal oxides (TMOs) such as TiO_2, ZnO, WO_3, α-Fe_2O_3, and SnO_2 have become high-performance and economically significant photoanode materials for efficient PEC water splitting. Owing to their unique d-electron structure, TMOs exhibit excellent stability, which facilitates electron transition between d-orbitals and thereby avoids the photocorrosion problem prone to occur in many polar semiconductors [23].

WO_3 is a promising TMO, featuring an appropriate energy band gap (~2.6 eV, enabling light absorption at wavelengths below 480 nm, far exceeding the light absorption range of TiO_2), a valence band edge location that is well-suited for water splitting (~3.0 V vs. RHE), a medium hole diffusion length(~150 nm; in contrast to merely 2–4 nm for α-Fe_2O_3), and an outstanding photogenerated carrier mobility(~12 $cm^2 \cdot V^{-1} \cdot s^{-1}$, versus 0.5 $cm^2 \cdot V^{-1} \cdot s^{-1}$ for TiO_2) [24,25]. The comparison table of key indicators for WO_3 versus $BiVO_4$, Fe_2O_3, and TiO_2 is shown in Table 1 (R2). Furthermore, non-stoichiometric tungsten oxide (WO_{3-x}) shows broad optical absorption spanning the ultraviolet (UV), visible (Vis), and near-infrared (NIR) regions [26]. In addition, the intense localized surface plasmon resonance (LSPR) effect of WO_{3-x} confers robust light absorption over a wide wavelength range in the near-infrared (NIR) spectrum [27]. Beyond these optical advantages, WO_3 also possesses several merits: adjustable morphology and composition, superior chemical stability under suitable pH conditions, comparatively lower toxicity relative to other metal oxides, and outstanding electrical conductivity.

However, WO_3-based photoanodes suffer from critical drawbacks in photocatalysis, among which the core problems are the relatively high conduction band minimum (CBM) potential and the extremely low separation efficiency of photogenerated carriers. Therefore, researchers have proposed numerous optimization and regulation strategies, including morphology control, doping, OER cocatalysts modification, heterostructure construction and SPR-enhanced surface modification strategy, etc. The above-mentioned optimization strategies are capable of boosting the efficient separation of photoinduced carriers, mobility of photogenerated carriers, and optical absorption efficiency. A step-by-step breakdown and detailed illustration of all the aforementioned techniques will be provided in Section 3 titled "Modification Strategy of Tungsten Oxide-based Photoanodes". And the schematic diagram illustrating the modification strategy of this article is shown in Figure 1. Finally, we will provide a summary and perspective on WO_3-based photoanodes.

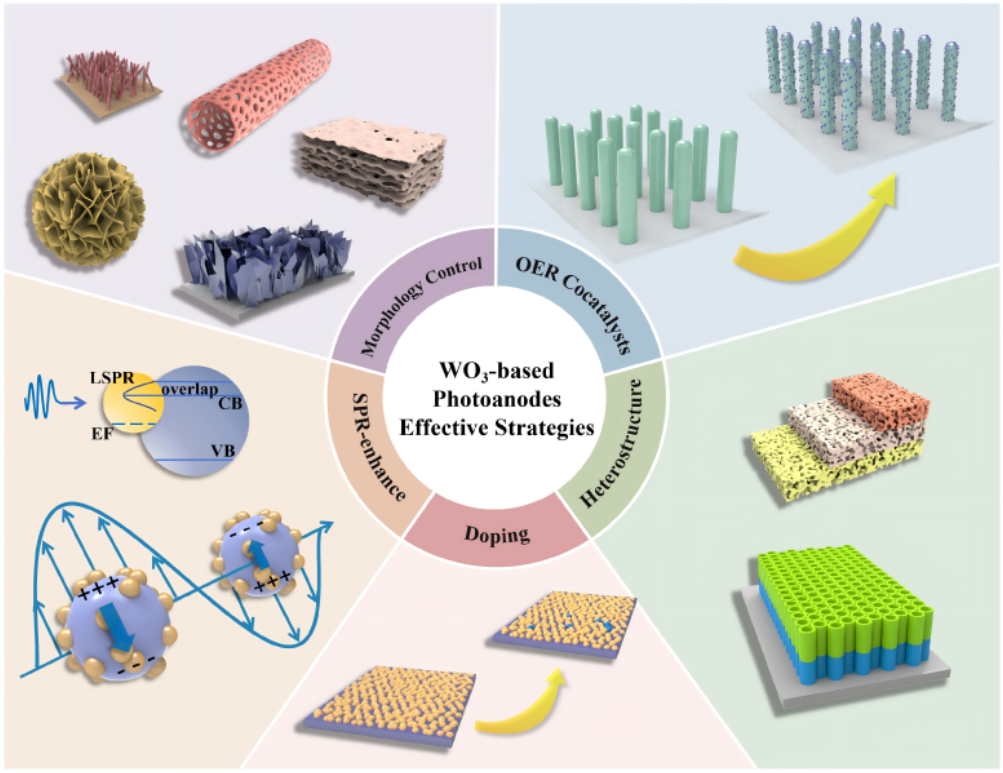

Figure 1. Schematic illustration of modification strategies for WO_3-based photoanodes.

Table 1. Comparison of key indicators between WO_3 and $BiVO_4$, Fe_2O_3, TiO_2.

Photoelectrode	Pristine Photocurrent ($mA \cdot cm^{-2}$)	Photocurrent ($mA \cdot cm^{-2}$)	Stability (h)	Faradaic Efficiency (Oxygen Evolution)	STH Efficiency (Theoretical/ Practical)	Ref
WO_3	2.0–4.0 at 1.23 V vs. RHE 0.5 M H_2SO_4	2.0–4.0 at 1.23 V vs. RHE 0.5 M H_2SO_4	200–500 (Acidic conditions)	85–95%	~5.0%/0.5–1.5%	[28]
$BiVO_4$	3.0–5.0 at 1.23 V vs. RHE	7.0–10.0 at 1.23 V vs. RHE	<200	80–90%	~9.0%/1.0–2.5%	[29,30]
Fe_2O_3	4.0–8.0 at 1.23 V vs. RHE	10.0–12.0 at 1.23 V vs. RHE	500–1000 (Stable in both acidic and alkaline conditions)	90–98%	~16.0%/1.5–3.0%	[31]
TiO_2	0.5–1.5 at 1.23 V vs. RHE	2.0–3.5 at 1.23 V vs. RHE	>1000	92–98%	~3.0%/0.1–0.5%	[31]

2. Fundamentals of PEC Water Splitting

To better understand the modification strategies of WO_3-based photoanodes, it is essential to clarify the basic principles of PEC water splitting. PEC represents an advanced oxidation technique that combines electrolysis and photocatalysis, where the system potential can be regulated to effectively enhance its comprehensive performance [32]. Compared with photocatalytic (PC) technology, PEC systems with an externally applied bias voltage can compensate for the potential deficit and overcome the energy barrier, which effectively promotes charge separation of photogenerated carriers and consequently delivers an enhanced Solar-to-Hydrogen (STH) conversion efficiency [33]. Meanwhile, PEC effectively addresses the limitations of PC water splitting, such as poor catalyst recoverability and the generation of H_2 and O_2 as mixed gases.

In the PEC water splitting system, semiconductors serve as electrode materials for light absorption. Figure 2 presents the simplified energy schematic of a PEC system constructed with an individual photoanode and a counter electrode. The band structure of the semiconductor consists of the conduction band (CB), bandgap (E_g) and valence band (VB). To enable the water oxidation reaction, the VB potential should be more anodic than the O_2/H_2O redox potential (1.23 V vs. RHE, pH = 0). Meanwhile, the CB potential needs to be more cathodic than H^+/H_2 redox potential (0 V vs. RHE) to drive the water reduction process. The overall water-splitting reaction is an endergonic uphill process, which requires Gibbs free energy change (ΔG) greater than 237 $kJ \cdot mol^{-1}$. Specifically, it mainly consists of three steps [34,35].

(1) Upon illumination with photons (hν) of energies greater than the bandgap (E_g), photogenerated electrons (e^-) are excited from the upper edge of the VB to the lower edge of the CB via interband transition and holes (h^+) are generated as empty states in the VB creating electron-hole pairs.
(2) The generated charge carriers are separated and transferred to the corresponding electrode surfaces. In general, electrons migrate toward the photocathode to undergo the hydrogen evolution reaction, while holes transfer to the photoanode surface for the oxygen evolution reaction.
(3) They participate in redox reactions on the surface of the photocatalyst. The photogenerated holes have extremely strong oxidizing properties and can react with water molecules to generate oxygen. And the photogenerated electrons have extremely strong reducing properties and can reduce water to hydrogen.

In most cases, the reaction of water splitting proceeds via two distinct half-reactions: the hydrogen evolution reaction (HER) and the oxygen evolution reaction (OER). Specifically as follows [36,37]:

$$\text{HER: } 2H^+ + 2e^- \rightarrow H_2 \text{ (0 V vs. NHE at pH 0)} \quad (1)$$

$$\text{OER: } 2H_2O \rightarrow O_2 + 2e^- + 2H^+ \text{ (1.23 V vs. NHE at pH 0)} \quad (2)$$

$$\text{Overall reaction: } 2H_2O \rightarrow 2H_2 + O_2 \quad (3)$$

(ΔE = 1.23 V; ΔG = 237.2 kJ/mol at 298 K and 1 atm).

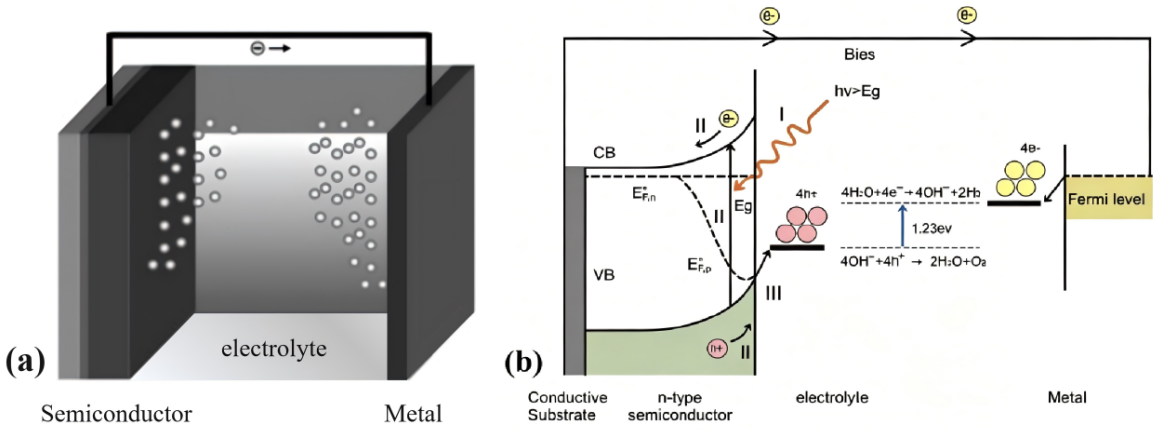

Figure 2. (**a**) Schematic diagram of PEC water splting system with n-type semiconductor photoanode and metal counter electrode [38] Copyright 2012, Springer Science+Business Media, LLC; (**b**) Corresponding energy band structure diagram [39] Copyright 2017, Royal Society of Chemistry.

3. Modification Strategy of WO_3-Based Photoanodes

Based on the above fundamental principles, five mainstream modification strategies have been developed to address the intrinsic drawbacks of pristine WO_3. In this section, five modification strategies for WO_3-based photocatalysts, namely morphology engineering, elemental doping, heterojunction construction, cocatalyst loading, and SPR modification, are compared and analyzed mechanistically. In terms of performance, heterojunction and cocatalyst modification afford the most significant enhancements, while cocatalyst loading and heterojunction construction exhibit the optimal stability. Their underlying mechanisms differ fundamentally: morphology engineering optimizes the physical structure, doping modifies the intrinsic electronic structure, heterojunctions boost charge separation via interfacial electric fields, cocatalysts improve surface reaction kinetics, and SPR modification relies on optical enhancement. Synergy among these strategies overcomes the limitations of single modification, yet each has inherent drawbacks; morphology engineering and non-noble metal cocatalyst loading show the best scalability. Overall, regulating charge dynamics and band structure is the core, and the ternary synergistic strategy combining morphology engineering, heterojunctions, and non-noble metal cocatalysts is a feasible scheme to promote the practical application of WO_3-based photoanodes [40,41]. Detailed studies on these modifications are analyzed in the following text.

3.1. Morphology Control

The dynamics of photogenerated charges that reach the surface are directly governed by the morphological features and architecture of photoanodes, and this represents a decisive factor controlling the efficiency of PEC reactions. Therefore, leveraging the synergy between nanoscale structural engineering and PEC properties has emerged as a key strategy for optimizing photoanode performance. WO_3 possesses low carrier mobilities and a short hole (minority carrier) diffusion length of approximately 150 nm, indicating that primarily the carriers generated within the depletion (space charge) layer contribute to the photocurrent. This requires the depletion layers to be wide enough to match the penetration depth of light [42]. Preparing WO_3 photoanodes with nanostructures can ensure that at least one dimension of them is less than the hole diffusion length and almost full coverage of the depletion layer, so that a higher proportion of photogenerated holes can contribute to OER [43]. One-dimensional (1D) nanostructures, (e.g., nanowires, nanotubes), two-dimensional (2D) nanosheets, three-dimensional (3D) porous nanostructures, etc. have been reported to demonstrate superior performance to reduce the probability of carrier recombination and enhance the photoelectric conversion efficiency [44].

The advantages of 1D nanostructures include a large specific surface area and superior charge transport, which allow efficient collection of charge carriers by the supporting substrate (e.g., FTO) and contribute to enhanced light absorption [45]. Kalanur et al. have realized the fabrication of vertically oriented WO_3 nanorods on transparent conductive substrates by a hydrothermal method that required no seed layers or structure directing agents. The optimized monoclinic WO_3 nanorod arrays annealed at 500 °C showed the highest photocurrent density [46]. Rao et al. have prepared WO_3 nanowires and nanotubes featuring high areal density and elongated length using flame vapor deposition (FVD) method to PEC water splitting, thus achieving improved light-harvesting absorption [47].

Furthermore, the specific surface area of 2D structures (such as nanosheets and nanofilms) is much higher than that of nanoparticles or 1D nanostructures, which can offer increased accessible active sites and enhance the contact interface between photoanodes and electrolyte. *Su* et al. have tailored WO_3 that exhibits morphologies from nanowires to nanoflake arrays by regulating the solution constituents, which grow along the (001) crystallographic orientation. The nanoflakes showed lower band gap values than the nanowires and improved the photocurrent significantly (a peak saturation photocurrent value of 1.43 $mA \cdot cm^{-2}$ under simulated AM 1.5G solar illumination) [48].

Different 3D nanostructures exhibit distinct light absorption and scattering properties. Common types include nanoflowers, nanoblocks, porous morphology, etc. Through a hydrothermal process with carboxylate ($RCOO^-$) serving as the structure-directing agent, Wang et al. have reported hexagonal nanoflower WO_3 arrays. Notably, the PEC activity of the nanoflower WO_3 photoanode was found to be almost three times superior to that of the pristine photoanode [49]. Wang et al. have constructed porous WO_3 PEC catalysts featuring low cost, high efficiency and structural robustness through a sol-gel process combined with high-temperature calcination, using polystyrene as the template. Impressively, annealed at 450 °C for 7 h in an oxygen atmosphere, the porous WO_3 photoanodes presented the most favorable PEC performance, whose IPCE value reaches 48.9% at 420 nm [50]. Several representative 1D, 2D, and 3D WO_3 nanostructures are illustrated in Figure 3. Meanwhile, the specific parameters of WO_3 samples with different morphologies are summarized in Table 2.

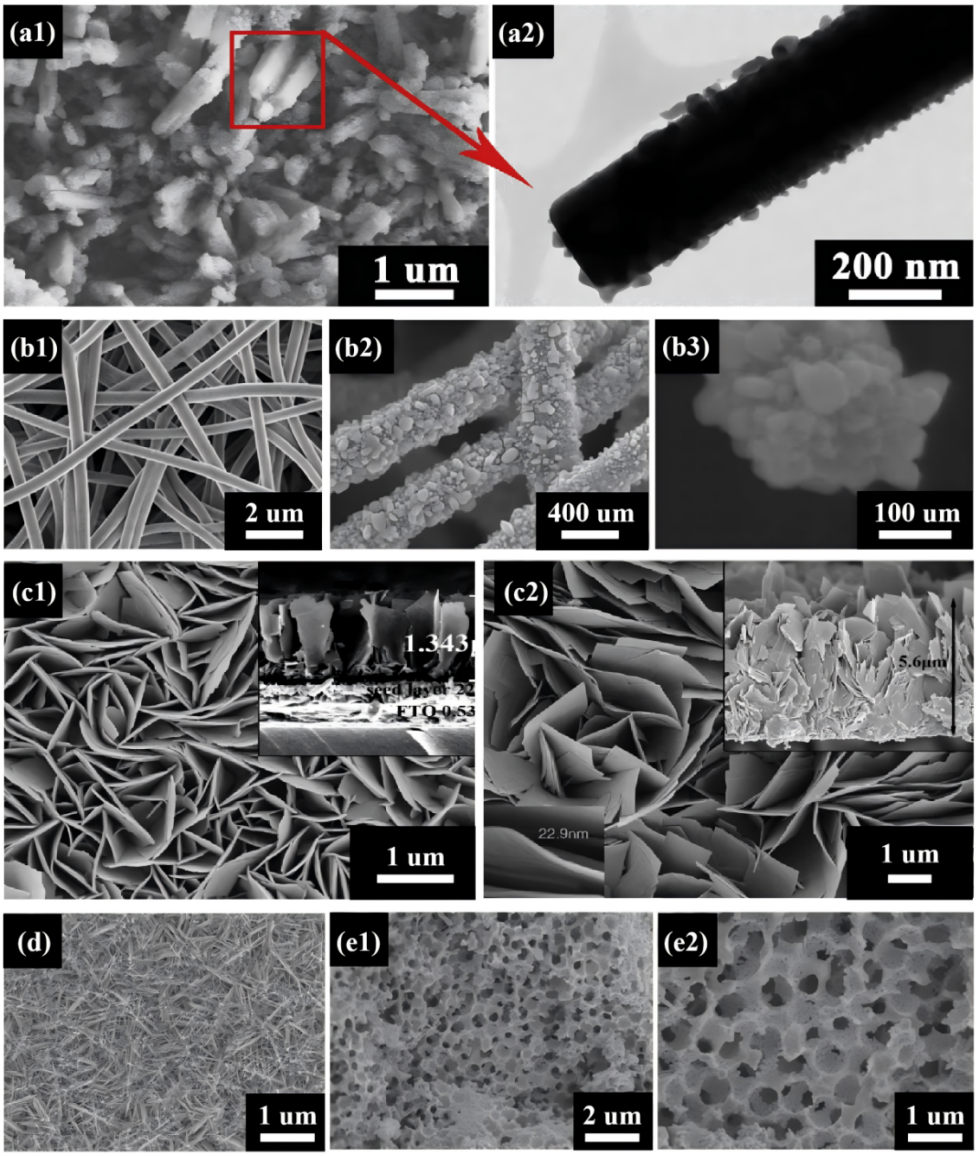

Figure 3. Morphology characterization of typical WO_3 nanostructures: (**a1**) SEM image of nanorods; (**a2**) TEM image of nanorods [51] Copyright 2016, Hydrogen Energy Publications LLC; (**b1**–**b3**) SEM images of nanofibers [52]; (**c1**–**c2**) FESEM images of nanoflake arrays; (**d**) SEM image of nanoneedles [53] Copyright 2014, Elsevier B.V.; (**e**) SEM image of porous structure [50] Copyright 2019, Elsevier Ltd. and Techna Group S.r.l.

Table 2. The detailed parameters of WO_3 of different morphologies.

Morphology	Method of Fabrication	Crystal Structure	Crystaline Orientation	Photocurrent (mA·cm^{-2})	Refs
Nanoneedle	Hydrothermal	Monoclinic	(020)	1.2 at 0.55V vs. RHE	[53]
Nanoplate film	Facile solvothermal	Monoclinic	(002) to (200)	0.08 at 0.4 V vs. SCE 0.5 M Na_2SO_4	[54]
Fe-doped nanofiber	Versatile electrospinning	Monoclinic	(020)	0.034 at 1.23 V vs. Ag/AgCl neutral sulphate electrolyte	[52]
Nano-grassblade	Hydrothermal	Monoclinic	(020)	1.2 at -0.1 V vs. SCE	[55]
Nanowire arrays to nanoflake arrays	Solvothermal	Hexagonal and monoclinic	Monoclinic: (002) to (200) Hexagonal:(001)	1.43~2 in 0.1 M Na_2SO_4	[48]
Nanosheet	Hydrothermal	Monoclinic	(002)	1.2 at 0.55V vs. Ag/AgCl	[43]
WO_3/Ag/CdS Nanorod	Hydrothermal	Monoclinic	(200)	1.38 at 0.6 V vs. Ag/AgCl	[51]
Nanorod	Hydrothermal	Monoclinic	(001)	2.26 at 1.23 V vs. 0.5 M Na_2SO_4	[46]
Nanotube and nanowire	Flame vapor deposition	Monoclinic		2.2 at 1.5 V vs. Pt	[47]
Nanoflower	Microwave-assisted hydrothermal	Hexagonal	[010] zone axis	~1.25 at 1.23 V vs. SEC 1 M H_2SO_4	[49]
Porous	sol-gel and high-temperature annealing		(002)	0.97 at 1.23 V vs. 0.5M Na_2SO_4	[50]

3.2. Doping

Doping in WO_3 enables the regulation of the CB and VB positions, the modulation of the band gap width, and the controllable introduction of lattice defect sites. This is conducive to accelerating the separation and transport of carriers by improving the electrical conductivity [56,57]. The elements selected for hetero atom doping can be classified into metallic elements and non-metallic elements. Lattice substitution with metal cations in catalysts serves as an effective way to enhance charge transport. Furthermore, inorganic semiconductors doped with nonmetallic elements can alter their electronic structures and optical absorption capacities, thereby improving the stability of their photoreactions [58]. Until now, various dopants have been employed for PEC water splitting and the detail of WO_3 of different dopants are listed in Table 3.

The incorporation of metal ions has emerged as a viable method for tailoring the physicochemical properties of WO_3 [59]. The energy level distributions of the CB (mainly composed of W 5d orbitals) and VB (mainly composed of O 2p orbitals) are usually changed by substituting W^{6+} (or interstitial doping) in the WO_3 lattice and utilizing the interactions between doped electronic configuration and lattice. The introduction of transition metal ions (e.g., Ti^{4+}, V^{5+}, Mo^{6+}) with ionic radii comparable to that of W^{6+} and slightly lower valence states can induce the formation of intermediate energy levels within the bandgap of WO_3 or result in hybridization with the 5d orbitals of W via their unfilled d orbitals. This process leads to an upward shift of the CBM or a shift of the valence band maximum (VBM), thereby narrowing the bandgap width [60,61]. Furthermore, introducing highly electronegative cations (e.g., Sn^{4+}, Nb^{5+}) can induce an upward shift of the CBM, enhancing the electron reduction ability of the conduction band [59,62].

Table 3. The detailed parameters of WO_3 doped with various elements.

Photoelectrode	Method	Optimal Doping Amount (at%)	Badgap (eV)	Photocurrent (mA·cm^{-2})	Pristine Photocurrent (mA·cm^{-2})	Refs
Ti-WO_3	Hydrothermal	1.16	2.73	1.16 at 1.23 V vs. RHE	0.335 at 1.23 V vs. RHE	[60]
Mo-WO_3	Hydrothermal	4.39	2.59	1.15 at 0.8 V vs.Ag/AgCl 0.1 M Na_2SO_4	0.23 at 0.8 V vs. Ag/AgCl 0.1 M Na_2SO_4	[63]
Bi-WO_3	Hydrothermal	0.17	2.24	1.511 at 1.23 V vs. RHE	0.401 at 1.23 V vs. RHE	[64]
Ag-WO_3	Spray pyrolysis	2	3.12			[65]
Ta-WO_3	Co-sputtering	3.93	2.61	0.65 at 1 V vs. Ag/AgCl	0.19 at 1 V vs. Ag/AgCl	[66]
Mn-WO_3	Hydrothermal	1.25	2.55	0.295 at 1.23 V vs. RHE	0.253 at 1.23 V vs. RHE	[67]
Fe-WO_3	Hydrothermal	0.51	2.45	0.442 at 1.23 V vs. RHE	0.253 at 1.23 V vs. RHE	[67]
Co-WO_3	Hydrothermal	0.41	2.51	0.636 at 1.23 V vs. RHE	0.253 at 1.23 V vs. RHE	[67]
Ni-WO_3	Hydrothermal	1.35	2.41	0.364 at 1.23 V vs. RHE	0.253 at 1.23 V vs. RHE	[67]
Cu-WO_3	Hydrothermal	1.34	2.45	0.487 at 1.23 V vs. RHE	0.253 at 1.23 V vs. RHE	[67]
Zn-WO_3	Hydrothermal	1.09	2.57	0.375 at 1.23 V vs. RHE	0.253 at 1.23 V vs. RHE	[67]
Sn-WO_3	Hydrothermal	0.8	2.46	0.427 at 1.23 V vs. RHE 0.5 M Na_2SO_4	0.253 at 1.23 V vs. RHE 0.5 M Na_2SO_4	[59]
Nb-WO_3	Hydrothermal condensation	2.12	2.58	0.414 at 1.23 V vs. RHE 0.5 M Na_2SO_4	0.3 at 1.23 V vs. RHE 0.5 M Na_2SO_4	[62]
C-WO_3	Spray-pyrolysis	1.1	2.57	1.6 at 1.8 V vs. Ag/AgCl 1 M HCl	0.5 at 1.8 V vs.Ag/AgCl 1 M HCl	[68]
S-WO_3	Hydrothermal	1.87	2.53	0.87 at 0.4 V vs. Ag/AgCl 0.5 M Na_2SO_4	0.62 at 0.4 V vs. Ag/AgCl 0.5 M Na_2SO_4	[69]
Fe/Sn co-doped WO_3	Flame-doping	Fe: 4.54 Sn: 0.22	2.42	1.45 at 1.23 V vs. RHE 0.5 M Na_2SO_3	0.24 at 1.23 V vs. RHE 0.5 M Na_2SO_3	[70]

Non-metallic element doping (such as S, N, C, and B) introduces defect energy levels within the bandgap by substituting O sites or occupying interstitial sites, thereby suppressing electron-hole recombination and inducing a redshift of the absorption edge as well as a narrowing of the band gap in the doped material [71,72]. However, single doping may have limitations such as enhanced carrier recombination and decreased stability, while co-doping can coordinate and balance band structure regulation and carrier behavior. Roh et al. have adopted a convenient one-step flame-doping method to realize the bidirectional co-doping of Fe and Sn into WO_3. Owing to dual-metal doping, the modified WO_3 shows a 6.16-fold higher photocurrent density at 1.23 V vs. RHE than that of the pristine sample [70].

3.3. OER Cocatalysts Modification

The cocatalysts (including heterogeneous and homogeneous cocatalysts) are conducive to promoting the interfacial charge transfer of photoelectrodes, thereby improving the photoelectrocatalytic performance of solar water splitting [73]. In PEC systems, the OER cocatalyst can effectively reduce the overpotential, increase the carrier utilization rate, accelerate the oxidation reaction kinetics and improve the stability of photocurrent [74]. Heterogeneous cocatalysts, predominantly solid nanoparticles (e.g., precious metals [75], metal oxides [76], metal sulfides [77]), are typically loaded on the surface of WO_3 to construct heterogeneous interfaces. And Table 4 presents specific detailed examples of co-catalysts that enhance photoelectrocatalytic performance.

Seabold et al. have observed the Co-Pi OER cocatalyst increase the photocurrent-oxygen conversion efficiency from roughly 61% up to almost 100% [78]. Cao et al. have deposited MnO_x onto the WO_3 photoanode via the photodeposition methods and achieved a maximum photocurrent density around 40% higher than that of the pristine one [79]. Zhang et al. have revealed that loading CoO_x can enhance the PEC performances resulting from the promoted charge carrier dynamics (separation and transport) and the accelerated kinetics of water oxidation [80]. There are also $LaFeO_3$ [81], Ca_2FeCoO_5 [82], etc. It is worth noting that amorphous oxyhydroxides have emerged in recent studies as high-performance cocatalysts in PEC catalysts [83–85]. Cai et al. developed a hydrothermal approach to realize conformal coating of ultra-thin Ni-doped FeOOH (Ni:FeOOH) OEC layers on various WO_3-based photoanodes and they exhibits a photocurrent density of 4.5 $mA \cdot cm^{-2}$ (1.23 VRHE, AM 1.5G) [86].

Table 4. The examples of co-catalysts that enhance photoelectrocatalytic performance.

Photoelectrode	OER Cocatalysts	Method	Photocurrent ($mA \cdot cm^{-2}$)	Pristine Photocurrent ($mA \cdot cm^{-2}$)	Refs
WO_3	Co-Pi	Electrodeposition	1.6 at 0.8 V vs. Ag/AgCl in 0.1 M KH_2PO_4	0.4 at 0.8 V vs. Ag/AgCl in 0.1 M KH_2PO_4	[78]
WO_3	MnO_x	Photodeposition and hydrothermal	higher than that of pristine WO_3 photoanode around 40%		[79]
$BiVO_4/WO_3$	CoO_x	Photodeposition	2.3 at 1.23 V vs. RHE	1.15 at 1.23 V vs. RHE	[80]
WO_3	Ni/Co-$LaFeO_3$	Electrodeposition	3.92 at 1.23 V vs. RHE	0.11 at 1.23 V vs. RHE	[81]
WO_3	Ca_2FeCoO_5	Sol−gel	the most active CFCO/WO_3 came close to those of RuO_2/WO_3 and Co-Pi/WO_3		[82]
$WO_3/BiVO_4$	FeOOH/NiOOH	Photodeposition and electrodeposition	5.35 ± 0.15 at 1.23 V vs. RHE in 0.5 M Na_2SO_4	3.9 at 1.23 V vs. RHE in 0.5 M Na_2SO_4	[83]
WO_3	FeOOH/NiOOH	Photodeposition	1.2 at 0.6 V vs. SCE	0.6 at 0.6 V vs. SCE	[84]
Zn-WO_3	FeOOH/CoOOH	Electrodeposition	3.63 at 1.23 V vs. RHE	1.49 at 1.23 V vs. RHE	[85]
$BiVO_4/WO_3$	F:FeOOH	Hydrothermal	3.1 at 1.23 V vs. RHE in 0.1 M KH_2PO_4	1.2 at 1.23 V vs. RHE in 0.1 M KH_2PO_4	[76]
$WO_3/BiVO_4$	Ni:FeOOH	Hydrothermal	4.5 at 1.23 V vs. RHE in 0.5 M KH_2PO_4		[86]
WO_3	CP-FeOx	Situ cogrowth			[87]
WO_3/CdS	NiS QDs	Hydrothermal			[88]
WO_3	$FeCl_2$	Impregnation	higher than that of pristine WO_3 photoanode around 60%		[88]

Notably, Lin et al. have proposed a configuration of 3D decoupling cocatalysts based on a crisscross, pore-spanning conducting polymer host, delivering notably boosted PEC activity [87]. Furthermore, quantum dots, endowed with size effect and quantum confinement effect, are capable of tuning light absorption and carrier transport properties, and thus can serve as cocatalysts for WO_3. Wang et al. have synthesized the NiS quantum dots loaded CdS/WO_3 composite furnished additional surface active sites for chemical reactions [89]. Homogeneous cocatalysts, usually soluble small molecules or ions (e.g., metal ions, organic complexes, etc.), can also accelerate the water oxidation reaction [90]. Klepser et al. have demonstrated combining $FeCl_2$ with WO_3 can significantly increase the reaction rate and selectivity of PEC water oxidation [88].

3.4. Heterostructure Construction

Some defects of single-component WO_3, for instance: a relatively large band gap prevents WO_3 from absorbing the vast proportion of the visible solar spectrum, can be improved by coupling other photoelectric semiconductors to improve the catalytic performance [53]. By exposing additional active sites and facilitating interfacial electron transfer, the construction of heterostructures realizes a 1 + 1 > 2 synergistic effect in PEC performance, a phenomenon termed the "spillover" mechanism of the system [91,92]. Common WO_3 heterostructures include $BiVO_4$, Fe_2O_3, TiO_2 and carbon quantum dots (CQDs), etc. Table 5 lists the fabrication approaches and photocurrent of some WO_3-based heterostructure photoelectrodes.

$BiVO_4$ (BVO), like WO_3, also stands out as a highly promising material for PEC system because of its 2.4 eV band gap, favorable band edge locations, and excellent long-term stability. Nevertheless, the PEC activity of BVO is not sufficient, primarily due to the poor electron transfer properties and the CB that lies higher than the H^+/H_2 redox potential [93]. The combination of BVO/WO_3 resulting in enhanced performance compared to single oxide photoanodes has been extensively studied [94]. Fang et al. have prepared a ternary $WO_3/BiVO_4$/NiOOH photoanode that showed a good photocurrent response of 3.00 $mA \cdot cm^{-2}$ (1.23 V vs. RHE) [95]. Also, the layer thickness of various photoanodes has a significant impact on PEC performance. Polo et al. have investigated the PEC performance of $WO_3/BiVO_4$ photoanodes with different thicknesses (WO_3 subjacent layer and $BiVO_4$ coating layer), identified the optimal thickness balance of the two oxides, and revealed that this balance minimizes charge recombination paths [96].

Table 5. Summary of synthesis methods and photocurrent of WO_3 heterostructure photoelectrodes.

Photoelectrode	Method	Photocurrent ($mA \cdot cm^{-2}$)	Pristine Photocurrent ($mA \cdot cm^{-2}$)	Refs
$WO_3/BiVO_4$	Solvothermal deposition and spincoating	0.8 at 0.4 V vs. RHE		[97]
$NiMoO_4$/ $BiVO_4$/Sn:WO_3	Hydrothermal and spin-coating	2.06 at 1.23 V vs. RHE in KBi electrolyte	0.55 at 1.23 V vs. RHE in KBi electrolyte	[94]
$BiVO_4$/Sn:WO_3	Hydrothermal and spin-coating	1.45 at 1.23 V vs. RHE in KBi electrolyte	0.55 at 1.23 V vs. RHE in KBi electrolyte	[94]
WO_3/Sb_2S_3	Hydrothermal	1.79 at 0.8 V vs. RHE	0.45 at 0.8 V vs. RHE	[98]
$WO_3/BiVO_4$/ NiOOH	Sol−gel and photoelectric deposition	2.92 at 1.23 V vs. RHE	0.42 at 1.23 V vs. RHE	[95]
$SnO_2/WO_3/BiVO_4$	Electron beam deposition and wet chemical	2.01 at 1.23 V vs. RHE	0.5 at 1.23 V vs. RHE	[99]
$WO_3/BiVO_4/BiFeO_3$	Sol−gel	6.3 at 2.5 V vs. RHE		[100]
$Fe_2O_3/TiO_2/WO_3/Ti_3C_2T_x$	GLAD and spin-coating	1.09 at 1.23 V vs. RHE		[101]
WO_3/α-Fe_2O_3	Hydrothermal	1.66 at 1.23 V vs. RHE	0.58 at 1.23 V vs. RHE	[102]
WO_3/Ti-Fe_2O_3	Hydrothermal	2.15 at 1.23 V vs. RHE	0.55 at 1.23 V vs. RHE	[103]
WO_3/α-Fe_2O_3/Bi_2S_3	Hydrothermal	5.777 at 1.0 V vs. RHE		[104]
CQDs/TiO_2/WO_3	Chemical bath deposition	2.03 at 1.23 V vs. RHE	0.9 at 1.23 V vs. RHE	[105]
CQDs/WO_3	Hydrothermal and immersing process	1.18 at 1.23 V vs. RHE	0.96 at 1.23 V vs. RHE	[106]
$WO_3/BiVO_4/TiO_2$	Hydrothermal, spin coating, and electrodeposition	4.2 at 1.23 V vs. RHE in 0.1 M Na_2SO_4	1.41 at 1.23 V vs. RHE in 0.1 M Na_2SO_4	[107]
N-CQDs/WO_3	Impregnation	1.42 at 1.0 V vs. RHE in 0.1 M Na_2SO_4	0.63 at 1.0 V vs. RHE in 0.1 M Na_2SO_4	[108]

α-Fe_2O_3 (the bandgap of 1.9~2.2 eV) has visible-light response, high chemical stability and economic efficiency, making it a promising material for visible-light-driven applications [109]. Fabrication of a WO_3/Fe_2O_3 heterojunction has been regarded as a viable strategy to enhance the PEC performance of WO_3, as it broadens the light harvesting spectral range and promotes the separation and transfer of photogenerated carriers [102]. And as a pioneering photocatalytic material, TiO_2 exhibits a wide bandgap (3.2 eV for anatase, 3.0 eV for rutile), outstanding resistance to photocorrosion, economical synthesis and excellent environmental friendliness. But its limited light absorption and rapid photoexcited carrier recombination restrict its application in PEC [101]. Besides forming a heterojunction with carbon quantum dots (CQDs) can effectively extend the visible-light absorption range and exhibit upconversion photoluminescence (PL) behavior. Meanwhile CQDs also possess outstanding advantages such as eco-friendliness, cost-effectiveness, industrial application potential and chemical stability [105]. Zhao et al. have fabricated the composite of vertical WO_3 NP and CQDs successfully and enhanced the photocurrent density [106].

3.5. SPR-Enhanced Surface Modification Strategy

The SPR effect refers to a phenomenon where free electrons on the surface of noble metals (For example, Au [110], Ag [111,112]) nanoparticles undergo collective oscillation under the action of incident light. Specifically, local surface plasmon resonance (LSPR) has emerged as a key strategy for optimizing the

photocatalytic performance of semiconductors due to its lack of propagation condition restrictions and the ability to generate strong local electromagnetic fields and light absorption effects at the nanoscale. Taking gold nanoparticles (Au NPs) as a paradigmatic illustration, this mechanism is delineated in Figure 4 [113].

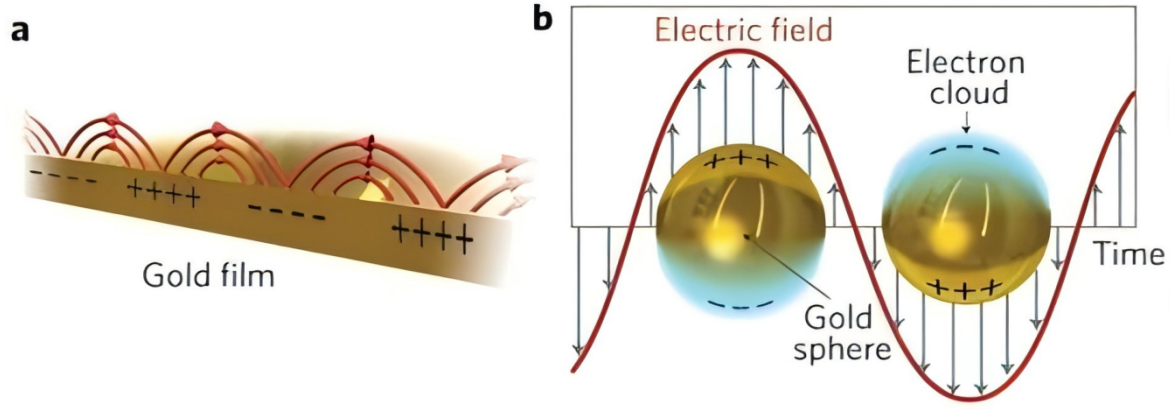

Figure 4. Schematic of plasmon resonance effects: (**a**) Propagating surface plasmon polariton (SPP) of Au thin film; (**b**) Localized surface plasmon (LSP) of Au nanoparticles [113]. Copyright 2018, Royal Society of Chemistry.

Tahir et al. have fabricated plasmonic Au incorporated WO_3/TiO_2 and confirmed that the Z-scheme and the Au-NPs SPR effect contribute to significantly enhancing the hydrogen production efficiency [114]. Ma et al. have reported the design of the Ag@WO_3 by the ultrasonic synthesis method to optimize the material's structural properties. Both the enriched hydrogen adsorption active sites endowed by a core-shell structure and the plasmon resonance effect originating from Ag nanoparticles (NPs) give rise to the enhanced photocatalytic HER performance [115]. In addition to metal nanoparticles, oxygen vacancies exhibit exceptional SPR effect in some semiconductor materials (such as mesoporous $WO_{2.83}$), which is capable of being widely tuned through redox-based chemical strategies [116]. Wei et al. have demonstrated that WO_{3-x} quantum dot decorated silver nanowire displayed both photocatalytic reactivity and surface-enhanced Raman scattering (SERS) properties. The observed synergistic effect is originated from the plasmonic state of WO_{3-x} quantum dot upon light irradiation [117]. Overall, the local strong electromagnetic field generated by the SPR effect acting on WO_3 can enhance the light absorption intensity of WO_3. Meanwhile, the Schottky barrier between the metal NPs and WO_3 facilitates the rapid transfer of the photogenerated electrons of WO_3 to the surface of the metal NPs, effectively preventing carrier recombination. Some effects of SPR enhancement are shown in Table 6.

Table 6. Summary of synthesis methods and effects of SPR-enhanced photoelectrodes.

Photoelectrode	Method	Effect	Refs
Au-NPs WO_3/TiO_2	Sol-gel assisted photodeposition	The maximum H_2 production yield was 17,200 ppm $h^{-1}\cdot g\cdot cat^{-1}$, which was 4.46 times that of WO_3/TiO_2	[114]
Ag-WO_3	Sonochemistry	10 mA cm^{-2} at 0.8 V vs. CSNSs	[113]
Meso-WO_3	Solid phase sintering	Overpotential: 287 mV (vs. RHE), significantly lower than that of pure electrodes	[116]
WO_{3-x} QD@Ag NW	Solvotherma	E_a decreases to 0.037 eV	[117]
WO_{3-x}/TiO_2	Radio frequency magnetron sputtering	0.2 mA cm^{-2} (approximately 0.025 mA$\cdot cm^{-2}$)	[112]
Pt-Ag/WO_3	Sol-gel	The electrochemical performance has been significantly improved	[118]

4. Computational Studies and Practical Applicability Evaluation

4.1. The Computational Studies on WO_3 for Water Splitting

Computational studies based on density functional theory (DFT) can effectively reveal the electronic structure, surface chemical properties and reaction mechanism of tungsten oxide-based semiconductors, and play a crucial role in guiding material design to improve performance. For instance, Hajiahmadi et al. screened the optimal surface structure and computational functional via DFT, and identified the OER pathway on the hexagonal WO_3 (h-WO_3) (001) surface for the first time, providing microscopic evidence for the surface engineering of WO_3

in water-splitting [119]. Muhammad et al. designed a combined Projector Augmented Wave-Perdew-Burke-Ernzerhof + van der Waals (PAW-PBE + vdW) scheme based on DFT first-principles calculations to compute the weak van der Waals interactions between Bi_2O_3 and WO_3, solving the problem that conventional PBE functionals underestimate weak interactions, and laying a methodological foundation for the structural design of WO_3-based composite materials [120]. Diaby et al. first applied artificial neural networks (ANN) to predict the PEC performance of WO_3-based photoanodes, and proposed two predictive models (the LMANN model and the SCGANN model), both of which achieved high consistency between experiments and theories, with the LMANN model showing superior fitting accuracy (as shown in Figure 5), providing a cross-disciplinary integrated idea for computational studies of WO_3-based semiconductors [121].

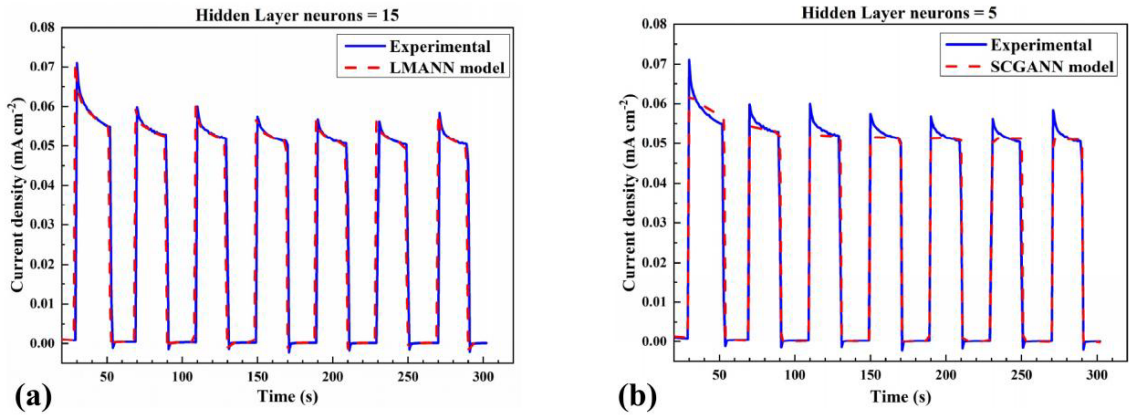

Figure 5. Photocurrent prediction of WO_3/SS photoanode using (**a**) LMANN and (**b**) SCGANN algorithms [121]. Copyright 2023, Multidisciplinary Digital Publishing Institute.

Nevertheless, current computational studies still have non-negligible limitations. One of the core problems is the disconnection between the oversimplified computational models and the actual systems. Hajiahmadi only focused on the ideal single (001) crystal plane for discussion, while the actual characteristics of WO_3, such as the coexistence of multiple crystal phases and the enrichment of defect structures, were not considered, making the computational results unconvincing. Moreover, the contradiction between computational efficiency and system scale restricts the development of computational research. Although Muhammad's combined scheme improved accuracy, the van der Waals (vdW) correction (especially the three-body many-body term) leads to a computational cost that increases with the number of atoms in an $O(n^3)$ manner. Finally, the universality of cross-disciplinary integrated models is questionable. Diaby's ANN model suffers from the "black-box dilemma" without embedded physical constraints (such as thermodynamic laws and size effects), and its fitting accuracy may decrease significantly when extended to multi-element doping or complex heterostructures. Therefore, future research needs to deepen the integration of DFT and artificial intelligence, construct a multiscale simulation framework, conduct dynamic simulations combined with actual service environments, form a computation-experiment closed loop, and promote the practical application of tungsten oxide materials.

4.2. Practical Applicability

There exists a striking gap between the performance optimization and small-batch preparation of materials in the laboratory and the complex service conditions as well as large-scale application demands in practical scenarios. As one of the core candidate materials for photoelectrocatalytic water splitting, WO_3 still requires evaluation and optimization of three critical issues, long-term stability and pH adaptability, scalability, and cost control, for its translation from laboratory research to practical application.

Long-term stability is the core prerequisite for the practical application of photoelectrocatalytic materials, and the problems of photocorrosion and structural reconstruction of WO_3-based photoanodes during service urgently need to be solved. Studies have demonstrated that the electrolyte pH exerts a significant influence on the stability of WO_3-based photoanodes. Under the synergistic action of light and electricity, WO_3 is relatively stable in acidic media but prone to tungsten dissolution; meanwhile, it undergoes facile alkaline chemical dissolution at pH > 4, making long-term service unfeasible [122–124]. Therefore, the stability of WO_3-based photoanodes in neutral electrolytes is also of great importance [25]. Knöppel et al. investigated the photocorrosion mechanism of WO_3 in acidic environments and proposed that sulfur-containing electrolytes are readily oxidized to form stable persulfate intermediates, which form strong complexes with W^{n+} and accelerate tungsten dissolution. By

comparing the performance of different acidic electrolytes, they identified HNO_3 as the electrolyte with the best photocorrosion resistance [122]. Jakubow-Piotrowska et al. confirmed via 80-h long-term PEC stability tests that mesoporous WO_3 photoanodes can maintain stable structure and PEC performance in 1 M aqueous methanesulfonic acid solution. This effectively addresses the long-term stability challenge of WO_3 photoanodes deactivating due to the formation of peroxo species in acidic water-splitting electrolytes and corrects the erroneous conclusions drawn from short-time experiments [125]. In the field of photoelectrocatalytic water splitting, a catalyst with 90% performance retention after 100 h of long-term testing at the laboratory stage represents excellent stability [126]. Nevertheless, it is still far from meeting the requirements for industrialization (approximately 1000 h of stable operation).

Small-area WO_3 photoelectrodes prepared in laboratories (typically 1 cm^2) can hardly meet the practical hydrogen production demands, and the development of scalable semiconductors while retaining their performance is a key challenge. Although traditional preparation methods such as hydrothermal and sol-gel methods can produce high-performance thin films, they suffer from unbalanced local reaction conditions, poor uniformity over large areas, and high fabrication costs, which directly compromise the catalytic performance. Atmospheric pressure chemical vapor deposition (APCVD) provides an effective route for the large-scale preparation of WO_3-based photoelectrodes. Tam et al. successfully fabricated large-scale scalable $WO_3/BiVO_4$ nanoheterojunction photoanodes for PEC water splitting using aerosol-assisted chemical vapor deposition (AACVD) at atmospheric pressure. After integrating with low-cost crystalline silicon photovoltaics (PV) in a tandem configuration, the solar-to-hydrogen (STH) conversion efficiency reached up to 3.2%. The fabrication process is vacuum-free, low-cost, and compatible with industrial mass production lines [127]. Cai et al. proposed a hybrid process combining ultrafast laser machining and thermal oxidation to fabricate in-situ grown WO_3 micro-nano structures on tungsten foils, providing a new route for the large-scale preparation and energy application of semiconductor oxide micro-nano structures [128]. Current processes for the large-scale preparation of WO_3 photoelectrodes are immature. For thin-film electrodes, the thickness deviation is required to be ≤5% with uniform distribution of active sites, which can be optimized by drawing on battery manufacturing processes. or powder catalysts, continuous hydrothermal synthesis can be carried out using industrial-grade reactors, and parameters such as feeding rate, reaction temperature, and stirring speed can be optimized to realize the ton-scale batch production of WO_3 powder.

The core of the cost issue lies in the reliance on noble metals. Although traditional cocatalysts such as Pt and RuO_2 can enhance catalytic activity, their high prices restrict large-scale applications, making the development of high-efficiency non-noble metal alternative systems the key [129]. Several low-cost cocatalysts have been discussed in Section 3.3. Through structural design and interface regulation, these cocatalysts can balance catalytic performance and cost, providing a feasible approach for cost control of WO_3-based catalysts. In addition, costs can be further reduced by optimizing raw material costs and controlling fabrication costs. For instance, industrial-grade tungsten sources (e.g., industrial tungstic acid, tungsten concentrate, and waste tungsten recycled materials) can be used to replace high-purity reagents. The price of industrial-grade raw materials is only 1/5 to 1/10 of that of high-purity reagents, but they may contain impurities such as iron, silicon, and calcium, whose effects on the catalytic performance of WO_3 need to be verified through experiments.

5. Summary and Outlook

The above discussion demonstrates that WO_3-based photoanodes have emerged as promising candidates for photoelectrocatalysts in PEC water splitting systems, and have motivated numerous research efforts by virtue of their unique advantages including low cost, excellent durability, favorable photoresponse, easy controllability of morphology and structure, and high compositional tunability. First off, we introduced the background of PEC hydrogen production, as well as the application advantages and existing problems of tungsten oxide-based photocatalysts. Secondly, the basic principles of the PEC water-splitting system centered on metal oxide photoanodes were discussed in detail. And following this, we provided a systematic overview of the tuning approaches for WO_3-based photoanodes over the past few years: morphology control, band structure engineering by doping, OER cocatalyst modification, heterostructure construction, and SPR-enhanced surface modification. Meanwhile, this review also elaborates on the fundamental principles and optimization effects of diverse effective strategies were also analyzed. Finally, we summarize the DFT-based computational studies and evaluate the practical applicability of WO_3 photoanodes.

In fact, the performance improvement of a single strategy on WO_3 is limited. The multi-strategy co-modification of the photoanode is more conducive to achieving efficient water decomposition in the PEC system. For instance, various effective strategies play distinct roles: morphology control provides a structural basis featuring multiple active sites and fast transport; doping enhances light utilization while increasing surface

reactivity; SPR effects enable the enhancement and broadening of light absorption; heterojunctions strengthen charge separation efficiency; OER cocatalysts loading accelerates the rate of surface reactions. The PEC behavior of TMOs will be significantly improved on a larger scale, approaching the requirements of commercial applications. We are optimistic that this review will inspire in-depth exploration of TMOs for high-performance PEC water splitting.

Author Contributions

(L.Z.) Lu Zhang: writing—original draft, methodology, investigation, formal analysis, data curation; C.W.: visualization, investigation; (L.Z.) Li Zhou: writing—review & editing; M.R.: conceptualization; Z.L.: writing—review & editing, supervision, funding acquisition. All authors have read and agreed to the published version of the manuscript.

Funding

This research was funded by National Natural Science Foundation of China (no. 52373301 and no. 22508289), Science Foundation of Tianjin (no. 23JCZDJC00180 and no. 25JCQNJC00260) and Joint Research Center of China and Foreign Countries Special Fund of Tianjin Innovation Platform (no. 24PTLYHZ00240).

Institutional Review Board Statement

Not applicable.

Informed Consent Statement

Not applicable.

Data Availability Statement

All data generated and analyzed in this study are available in this published article.

Conflicts of Interest

The authors declare no conflict of interest.

Use of AI and AI-Assisted Technologies

No AI tools were utilized for this paper.

References

1. Muradov, N.; Veziroglu, T. “Green” Path from Fossil-Based to Hydrogen Economy: An Overview of Carbon-Neutral Technologies. *Int. J. Hydrogen Energy* **2008**, *33*, 6804–6839.
2. Jacobson, M.Z. Review of Solutions to Global Warming, Air Pollution, and Energy Security. *Energy Environ. Sci.* **2009**, *2*, 148–173.
3. Shao, Q. Chemistry of Materials for Energy and Environmental Sustainability. *Molecules* **2024**, *29*, 5929.
4. Hosseini, S.E.; Andwari, A.M.; Wahid, M.A.; et al. A Review on Green Energy Potentials in Iran. *Renew. Sustain. Energy Rev.* **2013**, *27*, 533–545.
5. Xin, Z.; Zheng, H.; Hu, J. Construction of Hollow Co_3O_4@$ZnIn_2S_4$ p-n Heterojunctions for Highly Efficient Photocatalytic Hydrogen Production. *Nanomaterials* **2023**, *13*, 758.
6. Ouyang, J.; Sun, Y.; Zhang, Y.; et al. Tungsten Carbide/Tungsten Oxide Catalysts for Efficient Electrocatalytic Hydrogen Evolution. *Molecules* **2024**, *30*, 84.
7. Hosseini, S.E.; Wahid, M.A. Hydrogen Production from Renewable and Sustainable Energy Resources: Promising Green Energy Carrier for Clean Development. *Renew. Sustain. Energy Rev.* **2016**, *57*, 850–866.
8. Nikolaidis, P.; Poullikkas, A. A Comparative Overview of Hydrogen Production Processes. *Renew. Sustain. Energy Rev.* **2017**, *67*, 597–611.
9. Kimon, K.; Florian, F.; Andrea, D.R.; et al. *Global Energy and Climate Outlook 2022: Energy Trade in a Decarbonised World*; JRC Research Reports; Publications Office of the European Union: Luxembourg, 2022.
10. Wang, Q.; Domen, K. Particulate Photocatalysts for Light-Driven Water Splitting: Mechanisms, Challenges, and Design Strategies. *Chem. Rev.* **2019**, *120*, 919–985.
11. Fujishima, A.; Honda, K. Electrochemical Photolysis of Water at a Semiconductor Electrode. *Nature* **1972**, *238*, 37–38.

12. Han, J.; Liu, Z. Optimization and Modulation Strategies of Zinc Oxide-Based Photoanodes for Highly Efficient Photoelectrochemical Water Splitting. *ACS Appl. Energy Mater.* **2021**, *4*, 1004–1013.
13. Zheng, G.; Jiang, S.; Zhang, F.; et al. Synthesis and Characterization of WO_3 Photoanodes for Efficient Photoelectrochemical Water Splitting. *Appl. Phys. A* **2025**, *131*, 82.
14. Hu, X.; Huang, J.; Cao, Y.; et al. Photothermal-Boosted Polaron Transport in Fe_2O_3 Photoanodes for Efficient Photoelectrochemical Water Splitting. *Carbon Energy* **2023**, *5*, e369.
15. Kolodziejak, K.; Sar, J.; Wysmulek, K.; et al. Durability of $SrTiO_3$-TiO_2 Eutectic Composite as a Photoanode for Photoelectrochemical Water Splitting. *RSC Adv.* **2023**, *13*, 35422–35428.
16. Parangusan, H.; Bhadra, J.; Ahmad, Z.; et al. Hierarchical $BaTiO_3$/$NiFe_2O_4$ Nanocomposite as an Efficacious OER Catalyst for Photoelectrochemical Water Splitting. *Ceram. Int.* **2022**, *48*, 29136–29143.
17. Ye, Z.; Hu, Z.; Yang, L.; et al. Stable p-Type Cu:$CdS_{1-x}Se_x$/Pt Thin-Film Photocathodes with Fully Tunable Bandgap for Scavenger-Free Photoelectrochemical Water Splitting. *Sol. RRL* **2020**, *4*, 1900567.
18. Son, M.K. Key Strategies on Cu_2O Photocathodes toward Practical Photoelectrochemical Water Splitting. *Nanomaterials* **2023**, *13*, 3142.
19. Narangari, P.R.; Butson, J.D.; Tan, H.H.; et al. Surface-Tailored InP Nanowires via Self-Assembled Au Nanodots for Efficient and Stable Photoelectrochemical Hydrogen Evolution. *Nano Lett.* **2021**, *21*, 6967–6974.
20. Jena, A.; Chen, C.J.; Chang, H.; et al. Comprehensive View on Recent Developments in Hydrogen Evolution Using MoS_2 on a Si Photocathode: From Electronic to Electrochemical Aspects. *J. Mater. Chem. A* **2021**, *9*, 3767–3785.
21. Alqahtani, M.; Sathasivam, S.; Cui, F.; et al. Heteroepitaxy of GaP on Silicon for Efficient and Cost-Effective Photoelectrochemical Water Splitting. *J. Mater. Chem. A* **2019**, *7*, 8550–8558.
22. Wang, J.; Liu, K.; Liao, W.; et al. Metal Vacancies in Semiconductor Oxides Enhance Hole Mobility for Efficient Photoelectrochemical Water Splitting. *Nat. Catal.* **2025**, *8*, 229–238.
23. Bozheyev, F.; Nemkayeva, R.; Yerlanuly, Y.; et al. Performance of Transition Metal Oxides for Solar Hydrogen Conversion. *ACS Catal.* **2025**, *15*, 16449–16462.
24. Gaillard, N.; Kaneshiro, J.; Miller, E.L.; et al. Surface Modification of Tungsten Oxide-Based Photoanodes for Solar-Powered Hydrogen Production. *MRS Online Proc. Libr.* **2009**, *1171*, 1171-S02-01.
25. Chandra, D.; Ouchi, K.; Tsubonouchi, Y.; et al. Optically Transparent WO_3 Films with Organized Mesopores and Oriented Crystallinity: An Efficient and Robust Photoanode for Visible-Light-Driven Water Oxidation at Neutral pH. *Appl. Catal. B Environ. Energy* **2026**, *380*, 125733.
26. Chen, S.; Xiao, Y.; Xie, W.; et al. Facile Strategy for Synthesizing Non-Stoichiometric Monoclinic Structured Tungsten Trioxide (WO_{3-x}) with Plasma Resonance Absorption and Enhanced Photocatalytic Activity. *Nanomaterials* **2018**, *8*, 553.
27. Wu, C.M.; Naseem, S.; Chou, M.H.; et al. Recent Advances in Tungsten-Oxide-Based Materials and Their Applications. *Front. Mater.* **2019**, *6*, 49.
28. Long, Z.; Li, Q.; Zhang, C.; et al. $BiVO_4$/WO_{3-x} S-Scheme Heterojunctions with Amplified Internal Electric Field for Boosting Photothermal-Catalytic Activity. *Acta Phys. Chim. Sin.* **2025**, *41*, 100122.
29. Yang, N.; Zhang, S.; Xiao, Y.; et al. Insight into the Key Restriction of $BiVO_4$ Photoanodes Prepared by Pyrolysis Method for Scalable Preparation. *Angew. Chem. Int. Ed.* **2023**, *62*, e202308729.
30. Fan, M.; Tao, Z.; Zhao, Q.; et al. Molecular Copper Phthalocyanine and FeOOH Modified $BiVO_4$ Photoanodes for Enhanced Photoelectrochemical Water Oxidation. *Adv. Mater. Technol.* **2023**, *8*, 2201835.
31. Krysa, J.; Zlamal, M.; Kment, S.; et al. TiO_2 and Fe_2O_3 Films for Photoelectrochemical Water Splitting. *Molecules* **2015**, *20*, 1046–1058.
32. Cifre-Herrando, M.; Roselló-Márquez, G.; Navarro-Gázquez, P.J.; et al. Characterization and Comparison of WO_3/WO_3-MoO_3 and TiO_2/TiO_2-ZnO Nanostructures for Photoelectrocatalytic Degradation of the Pesticide Imazalil. *Nanomaterials* **2023**, *13*, 2584.
33. Chen, X.; Zhang, Z.; Chi, L.; et al. Recent Advances in Visible-Light-Driven Photoelectrochemical Water Splitting: Catalyst Nanostructures and Reaction Systems. *Nano Micro Lett.* **2015**, *8*, 1–12.
34. Raub, A.A.M.; Bahru, R.; Nashruddin, S.N.A.M.; et al. Advances of Nanostructured Metal Oxide as Photoanode in Photoelectrochemical (PEC) Water Splitting Application. *Heliyon* **2024**, *10*, e39079.
35. Cao, S.; Piao, L.; Chen, X. Emerging Photocatalysts for Hydrogen Evolution. *Trends Chem.* **2020**, *2*, 57–70.
36. Wondimu, T.H.; Bayeh, A.W.; Kabtamu, D.M.; et al. Recent Progress on Tungsten Oxide-Based Materials for the Hydrogen and Oxygen Evolution Reactions. *Int. J. Hydrogen Energy* **2022**, *47*, 20378–20397.
37. Wu, Y.; Li, J.; Chong, W.K.; et al. Novel Materials and Techniques for Photocatalytic Water Splitting Developed by Professor Kazunari Domen. *Chin. J. Catal.* **2025**, *68*, 1–50.
38. van de Krol, R.; Grätzel, M. *Photoelectrochemical Hydrogen Production*; Springer: New York, NY, USA, 2012.
39. Jiang, C.; Moniz, S.J.A.; Wang, A.; et al. Photoelectrochemical Devices for Solar Water Splitting—Materials and Challenges. *Chem. Soc. Rev.* **2017**, *46*, 4645–4660.

40. Amer, M.S.; Arunachalam, P.; Al-Mayouf, A.M.; et al. Mesoporous Tungsten Trioxide Photoanodes Modified with Nitrogen-Doped Carbon Quantum Dots for Enhanced Oxygen Evolution Photo-Reaction. *Nanomaterials* **2019**, *9*, 1502.
41. Abduvalov, A.; Zhumanova, K.; Kaikanov, M.; et al. Photoactivity Enhancement of WO_3 Photoanodes Using the Combined Effect of Plasmonic Au and Photoluminescent Y_2O_3:Eu^{3+} Nanoparticles. *ACS Omega* **2024**, *9*, 46834–46840.
42. Santato, C.; Ulmann, M.; Augustynski, J. Enhanced Visible Light Conversion Efficiency Using Nanocrystalline WO_3 Films. *Adv. Mater.* **2001**, *13*, 511–514.
43. Qin, D.D.; Tao, C.L.; Friesen, S.A.; et al. Dense Layers of Vertically Oriented WO_3 Crystals as Anodes for Photoelectrochemical Water Oxidation. *Chem. Commun.* **2012**, *48*, 729–731.
44. Xu, Y.; Li, A.; Yao, T.; et al. Strategies for Efficient Charge Separation and Transfer in Artificial Photosynthesis of Solar Fuels. *ChemSusChem* **2017**, *10*, 4277–4305.
45. Lin, Y.; Yuan, G.; Liu, R.; et al. Semiconductor Nanostructure-Based Photoelectrochemical Water Splitting: A Brief Review. *Chem. Phys. Lett.* **2011**, *507*, 209–215.
46. Kalanur, S.S.; Hwang, Y.J.; Chae, S.Y.; et al. Facile Growth of Aligned WO_3 Nanorods on FTO Substrate for Enhanced Photoanodic Water Oxidation Activity. *J. Mater. Chem. A* **2013**, *1*, 3479.
47. Rao, P.M.; Cho, I.S.; Zheng, X. Flame Synthesis of WO_3 Nanotubes and Nanowires for Efficient Photoelectrochemical Water-Splitting. *Proc. Combust. Inst.* **2013**, *34*, 2187–2195.
48. Su, J.; Feng, X.; Sloppy, J.D.; et al. Vertically Aligned WO_3 Nanowire Arrays Grown Directly on Transparent Conducting Oxide Coated Glass: Synthesis and Photoelectrochemical Properties. *Nano Lett.* **2010**, *11*, 203–208.
49. Wang, N.; Wang, D.; Li, M.; et al. Photoelectrochemical Water Oxidation on Photoanodes Fabricated with Hexagonal Nanoflower and Nanoblock WO_3. *Nanoscale* **2014**, *6*, 2061.
50. Wang, Y.; Zhang, F.; Zhao, G.; et al. Porous WO_3 Monolith-Based Photoanodes for High-Efficient Photoelectrochemical Water Splitting. *Ceram. Int.* **2019**, *45*, 7302–7308.
51. Liu, Z.; Wu, J.; Zhang, J. Quantum Dots and Plasmonic Ag Decorated WO_3 Nanorod Photoanodes with Enhanced Photoelectrochemical Performances. *Int. J. Hydrogen Energy* **2016**, *41*, 20529–20535.
52. Song, K.; Ma, Z.; Yang, W.; et al. Electrospinning WO_3 Nanofibers with Tunable Fe-Doping Levels towards Efficient Photoelectrochemical Water Splitting. *J. Mater. Sci. Mater. Electron.* **2018**, *29*, 8338–8346.
53. Jin, T.; Diao, P.; Wu, Q.; et al. WO_3 Nanoneedles/α-Fe_2O_3/Cobalt Phosphate Composite Photoanode for Efficient Photoelectrochemical Water Splitting. *Appl. Catal. B Environ.* **2014**, *148–149*, 304–310.
54. Zhang, W.; Chen, H.; Peng, Q.; et al. Controlled Fabrication of WO_3 Nanoplate Films and Its Photoelectrochemical Properties. *Mater. Res. Express* **2019**, *6*, 095901.
55. Jin, T.; Xu, D.; Diao, P.; et al. Tailored Preparation of WO_3 Nano-Grassblades on FTO Substrate for Photoelectrochemical Water Splitting. *CrystEngComm* **2016**, *18*, 6798–6808.
56. Wang, F.; Di Valentin, C.; Pacchioni, G. Rational Band Gap Engineering of WO_3 Photocatalyst for Visible Light Water Splitting. *ChemSusChem* **2012**, *4*, 476–478.
57. Liu, X.; Wang, F.; Wang, Q. Nanostructure-Based WO_3 Photoanodes for Photoelectrochemical Water Splitting. *Phys. Chem. Chem. Phys.* **2012**, *14*, 7894–7911.
58. Yang, L.; Li, F.; Xiang, Q. Advances and Challenges in the Modification of Photoelectrode Materials for Photoelectrocatalytic Water Splitting. *Mater. Horiz.* **2024**, *11*, 1638–1657.
59. Kalanur, S.S. Structural, Optical, Band Edge and Enhanced Photoelectrochemical Water Splitting Properties of Tin-Doped WO_3. *Catalysts* **2019**, *9*, 456.
60. Kalanur, S.S.; Yoo, I.-H.; Seo, H. Fundamental Investigation of Ti Doped WO_3 Photoanode and Their Influence on Photoelectrochemical Water Splitting Activity. *Electrochim. Acta* **2017**, *254*, 348–357.
61. Majeed Khan, M.A.; Pawar, M.; Ansari, A.A.; et al. Boosted Photocatalytic and Electrochemical Activity of Hydrothermally Synthesized WO_3 Nanoparticles Co-doped with Transition Elements (Mn, Co). *Mater. Sci. Eng. B* **2024**, *307*, 117541.
62. Kalanur, S.S.; Yoo, I.H.; Cho, I.S.; et al. Niobium Incorporated WO_3 Nanotriangles: Band Edge Insights and Improved Photoelectrochemical Water Splitting Activity. *Ceram. Int.* **2019**, *45*, 8157–8165.
63. Kalanur, S.S.; Seo, H. Influence of Molybdenum Doping on the Structural, Optical and Electronic Properties of WO_3 for Improved Solar Water Splitting. *J. Colloid Interface Sci.* **2018**, *509*, 440–447.
64. Kalanur, S.S.; Yoo, I.H.; Eom, K.; et al. Enhancement of Photoelectrochemical Water Splitting Response of WO_3 by Means of Bi Doping. *J. Catal.* **2018**, *357*, 127–137.
65. Arifuzzaman, M.; Saha, T.; Podder, J.; et al. Effect of Silver Doping on the Band Gap Tuning of Tungsten Oxide Thin Films for Optoelectronic Applications. *Heliyon* **2024**, *10*, e27761.
66. Jafarpour, S.; Naghshara, H. Reactive Co-Sputter Deposition of Ta-Doped Tungsten Oxide Thin Films for Water Splitting Application. *Sci. Rep.* **2025**, *15*, 8302.
67. Kalanur, S.S.; Noh, Y.G.; Seo, H. Engineering Band Edge Properties of WO_3 with Respect to Photoelectrochemical Water Splitting Potentials via a Generalized Doping Protocol of First-Row Transition Metal Ions. *Appl. Surf. Sci.* **2020**, *509*, 145253.

68. Sun, Y.; Murphy, C.J.; Reyes-Gil, K.R.; et al. Photoelectrochemical and Structural Characterization of Carbon-Doped WO_3 Films Prepared via Spray Pyrolysis. *Int. J. Hydrogen Energy* **2009**, *34*, 8476–8484.
69. Li, W.; Li, J.; Wang, X.; et al. Preparation and Water-Splitting Photocatalytic Behavior of S-Doped WO_3. *Appl. Surf. Sci.* **2012**, *263*, 157–162.
70. Roh, S.H.; Kim, J.; So, W.; et al. Rapid Flame Induced Dual-Metal Doping on WO_3 Electrode for Boosting Photo-Electrochemical Water Oxidation. *Energy Mater.* **2025**, *5*, 500128.
71. Zych, M.; Syrek, K.; Pisarek, M.; et al. Synthesis and Characterization of Anodic WO_3 Layers in Situ Doped with C, N during Anodization. *Electrochim. Acta* **2022**, *411*, 140061.
72. Varga, T.; Haspel, H.; Kormányos, A.; et al. Nitridation of One-Dimensional Tungsten Oxide Nanostructures: Changes in Structure and Photoactivity. *Electrochim. Acta* **2017**, *256*, 299–306.
73. Li, D.; Shi, J.; Li, C. Transition-Metal-Based Electrocatalysts as Cocatalysts for Photoelectrochemical Water Splitting: A Mini Review. *Small* **2018**, *14*, 1704179.
74. Xiao, Y.; Fu, J.; Pihosh, Y.; et al. Interface Engineering for Photoelectrochemical Oxygen Evolution Reaction. *Chem. Soc. Rev.* **2025**, *54*, 1268–1317.
75. Higashimoto, S.; Kurikawa, Y.; Tanabe, Y.; et al. Photocatalytic Property of WO_3 Modified with Noble Metal Co-Catalysts towards Selective Hydroxylation of Benzene to Phenol under Visible Light Irradiation. *Appl. Catal. B Environ.* **2023**, *325*, 122289.
76. Li, Y.; Mei, Q.; Liu, Z.; et al. Fluorine-Doped Iron Oxyhydroxide Cocatalyst: Promotion on the WO_3 Photoanode Conducted Photoelectrochemical Water Splitting. *Appl. Catal. B Environ.* **2022**, *304*, 120995.
77. Villa, K.; Domènech, X.; García-Pérez, U.M.; et al. Photocatalytic Hydrogen Production Under Visible Light by Using a CdS/WO_3 Composite. *Catal. Lett.* **2015**, *146*, 100–108.
78. Seabold, J.A.; Choi, K.S. Effect of a Cobalt-Based Oxygen Evolution Catalyst on the Stability and the Selectivity of Photo-Oxidation Reactions of a WO_3 Photoanode. *Chem. Mater.* **2011**, *23*, 1105–1112.
79. Cao, X.; Zang, X.; Zhou, X.; et al. Rationally Designed/Constructed MnO_x/WO_3 Anode for Photoelectrochemical Water Oxidation. *Chin. Chem. Lett.* **2018**, *29*, 811–814.
80. Zhang, L.; Yang, M.; Luo, Z.; et al. Photodeposited CoO_x as Highly Active Phases to Boost Water Oxidation on $BiVO_4$/WO_3 Photoanode. *Int. J. Hydrogen Energy* **2019**, *44*, 25652–25661.
81. Li, Y.; Tang, S.; Sheng, H.; et al. Multiple Roles for $LaFeO_3$ in Enhancing the Photoelectrochemical Performance of WO_3. *J. Colloid Interface Sci.* **2023**, *629*, 598–609.
82. Tsuji, E.; Degami, Y.; Okada, H.; et al. Improvement of Photoelectrocatalytic Activity and Stability of WO_3 for Oxygen Photoevolution Reaction by Loading of Brownmillerite-Type Ca_2FeCoO_5 as a Cocatalyst. *Energy Technol.* **2021**, *9*, 2100197.
83. Shi, X.; Choi, I.Y.; Zhang, K.; et al. Efficient Photoelectrochemical Hydrogen Production from Bismuth Vanadate-Decorated Tungsten Trioxide Helix Nanostructures. *Nat. Commun.* **2014**, *5*, 4775.
84. Li, L.; Xiao, S.; Li, R.; et al. Nanotube Array-Like WO_3 Photoanode with Dual-Layer Oxygen-Evolution Cocatalysts for Photoelectrocatalytic Overall Water Splitting. *ACS Appl. Energy Mater.* **2018**, *1*, 6871–6880.
85. Li, X.; Ai, M.; Zhang, X.; et al. Dual Co-Catalysts Decorated Zn-WO_3 Nanorod Arrays with Highly Efficient Photoelectrocatalytic Performance. *Int. J. Hydrogen Energy* **2022**, *47*, 13641–13653.
86. Cai, L.; Zhao, J.; Li, H.; et al. One-Step Hydrothermal Deposition of Ni:FeOOH onto Photoanodes for Enhanced Water Oxidation. *ACS Energy Lett.* **2016**, *1*, 624–632.
87. Lin, H.; Long, X.; An, Y.; et al. Three-Dimensional Decoupling Co-Catalyst from a Photoabsorbing Semiconductor as a New Strategy to Boost Photoelectrochemical Water Splitting. *Nano Lett.* **2018**, *19*, 455–460.
88. Klepser, B.M.; Bartlett, B.M. Anchoring a Molecular Iron Catalyst to Solar-Responsive WO_3 Improves the Rate and Selectivity of Photoelectrochemical Water Oxidation. *J. Am. Chem. Soc.* **2014**, *136*, 1694–1697.
89. Wang, S.; Jiao, Y.; Yin, J.; et al. Innovation Synthesis of NiS Quantum Dots Modified CdS/WO_3 Heterostructures as High-Efficiency Bifunctional Photocatalysts for Construction of Visible Light Driven Z-Scheme Water-Splitting and Cr(VI) Degradation. *Appl. Surf. Sci.* **2022**, *602*, 154226.
90. Huang, J.; Yue, P.; Wang, L.; et al. A Review on Tungsten-Trioxide-Based Photoanodes for Water Oxidation. *Chin. J. Catal.* **2019**, *40*, 1408–1420.
91. Wang, Y.; Wang, R.; Duan, S. Optimization Methods of Tungsten Oxide-Based Nanostructures as Electrocatalysts for Water Splitting. *Nanomaterials* **2023**, *13*, 1727.
92. Puntsagdorj, S.; Koirala, A.R.; Gombovanjil, J.; et al. Increase in Photocurrent Density of WO_3 Photoanode by Placing a Layer of an Ordered Array of Mesoporous WO_3 Micropillars on Top of a WO_3 Sheet Layer. *ACS Appl. Mater. Interfaces* **2022**, *14*, 31838–31850.
93. Ali, M.; Pervaiz, E.; Sikandar, U.; et al. A Review on the Recent Developments in Zirconium and Carbon-Based Catalysts for Photoelectrochemical Water-Splitting. *Int. J. Hydrogen Energy* **2021**, *46*, 18257–18283.

94. Htet, H.T.; Jung, Y.; Kim, Y.; et al. Enhanced Photoelectrochemical Water Splitting Using $NiMoO_4$/$BiVO_4$/Sn-Doped WO_3 Double Heterojunction Photoanodes. *ACS Appl. Mater. Interfaces* **2024**, *16*, 52383–52392.
95. Fang, W.; Lin, Y.; Xv, R.; et al. Boosting Photoelectrochemical Performance of $BiVO_4$ Photoanode by Synergistic Effect of WO_3/$BiVO_4$ Heterojunction Construction and NiOOH Water Oxidation Cocatalyst Modification. *ACS Appl. Energy Mater.* **2022**, *5*, 11402–11412.
96. Polo, A.; Nomellini, C.; Marra, G.; et al. WO_3/$BiVO_4$ Heterojunction Photoanodes: Optimized Photoelectrochemical Performance in Relation to Both Oxides Layer Thickness. *Catal. Today* **2025**, *446*, 115137.
97. Fan, H.; Ding, Y.; Yan, W.; et al. Nanostructured WO_3/$BiVO_4$ Heterojunction Films Embedded with Au Nanoparticles for Efficient Photoelectrochemical Water Splitting. *MRS Commun.* **2021**, *11*, 295–301.
98. Zhang, J.; Liu, Z.; Liu, Z. Novel WO_3/Sb_2S_3 Heterojunction Photocatalyst Based on WO_3 of Different Morphologies for Enhanced Efficiency in Photoelectrochemical Water Splitting. *ACS Appl. Mater. Interfaces* **2016**, *8*, 9684–9691.
99. Bhat, S.S.M.; Lee, S.A.; Suh, J.M.; et al. Triple Planar Heterojunction of SnO_2/WO_3/$BiVO_4$ with Enhanced Photoelectrochemical Performance under Front Illumination. *Appl. Sci.* **2018**, *8*, 1765.
100. Khoomortezaei, S.; Abdizadeh, H.; Golobostanfard, M.R. Triple Layer Heterojunction WO_3/$BiVO_4$/$BiFeO_3$ Porous Photoanode for Efficient Photoelectrochemical Water Splitting. *ACS Appl. Energy Mater.* **2019**, *2*, 6428–6439.
101. Wu, S.; Ou, K.; Zhang, W.; et al. Fe_2O_3/TiO_2/WO_3/$Ti_3C_2T_x$ Heterojunction Composite Material for Efficient Photoelectrochemical Water Splitting. *Appl. Phys. A* **2024**, *130*, 155.
102. Li, Y.; Zhang, L.; Liu, R.; et al. WO_3@α-Fe_2O_3 Heterojunction Arrays with Improved Photoelectrochemical Behavior for Neutral pH Water Splitting. *ChemSusChem* **2016**, *8*, 2765–2770.
103. Wu, Q.; Bu, Q.; Li, S.; et al. Enhanced Interface Charge Transfer via n-n WO_3/Ti–Fe_2O_3 Heterojunction Formation for Water Splitting. *J. Alloys Compd.* **2019**, *803*, 1105–1111.
104. Tezca, F.; Ahma, A.; Kardas, G. WO_3/α-Fe_2O_3/Bi_2S_3 Ternary Photoanode for Improved Oxygen Evolution Reaction in Photoelectrochemical Water Splitting. *Turk. J. Chem.* **2025**, *49*, 176–190.
105. Wang, J.; Zhou, T.; Zhang, Y.; et al. The Design of High Performance Photoanode of CQDs/TiO_2/WO_3 Based on DFT Alignment of Lattice Parameter and Energy Band, and Charge Distribution. *J. Colloid Interface Sci.* **2021**, *600*, 828–837.
106. Zhao, Z.; Butburee, T.; Peerakiatkhajohn, P.; et al. Carbon Quantum Dots Sensitized Vertical WO_3 Nanoplates with Enhanced Photoelectrochemical Properties. *ChemistrySelect* **2016**, *1*, 2772–2777.
107. Kalanur, S.S.; Yoo, I.-H.; Park, J.; et al. Insights into the Electronic Bands of WO_3/$BiVO_4$/TiO_2, Revealing High Solar Water Splitting Efficiency. *J. Mater. Chem. A* **2017**, *5*, 1455–1461.
108. Kong, W.; Zhang, X.; Liu, S.; et al. N Doped Carbon Dot Modified WO_3 Nanoflakes for Efficient Photoelectrochemical Water Oxidation. *Adv. Mater. Interfaces* **2018**, *6*, 1801653.
109. Zhao, J. Excellent Photocatalytic Degradation and Antibiosis of WO_3/Fe_2O_3 Heterojunction. *Mater. Res. Express* **2022**, *9*, 055010.
110. Hu, D.; Diao, P.; Xu, D.; et al. Gold/WO_3 Nanocomposite Photoanodes for Plasmonic Solar Water Splitting. *Nano Res.* **2016**, *9*, 1735–1751.
111. Salimi, R.; Alvani, A.A.S.; Mei, B.T.; et al. Ag-Functionalized $CuWO_4$/WO_3 Nanocomposites for Solar Water Splitting. *New J. Chem.* **2019**, *43*, 2196–2203.
112. Gelija, D.; Loka, C.; Goddati, M.; et al. Integration of Ag Plasmonic Metal and WO_3/InGaN Heterostructure for Photoelectrochemical Water Splitting. *ACS Appl. Mater. Interfaces* **2023**, *15*, 34883–34894.
113. Huang, W.; Wang, J.; Bian, L.; et al. Oxygen Vacancy Induces Self-Doping Effect and Metalloid LSPR in Non-Stoichiometric Tungsten Suboxide Synergistically Contributing to the Enhanced Photoelectrocatalytic Performance of WO_{3-x}/TiO_{2-x} Heterojunction. *Phys. Chem. Chem. Phys.* **2018**, *20*, 17268–17278.
114. Tahir, M.; Siraj, M.; Tahir, B.; et al. Au-NPs Embedded Z-Scheme WO_3/TiO_2 Nanocomposite for Plasmon-Assisted Photocatalytic Glycerol-Water Reforming towards Enhanced H_2 Evolution. *Appl. Surf. Sci.* **2020**, *503*, 144344.
115. Ma, J.; Ma, Z.; Liu, B.; et al. Composition of Ag-WO_3 Core-Shell Nanostructures as Efficient Electrocatalysts for Hydrogen Evolution Reaction. *J. Solid State Chem.* **2019**, *271*, 246–252.
116. Cheng, H.; Klapproth, M.; Sagaltchik, A.; et al. Ordered Mesoporous $WO_{2.83}$: Selective Reduction Synthesis, Exceptional Localized Surface Plasmon Resonance and Enhanced Hydrogen Evolution Reaction Activity. *J. Mater. Chem. A* **2018**, *6*, 2249–2256.
117. Wei, W.; Yao, Y.; Zhao, Q.; et al. Oxygen Defect-Induced Localized Surface Plasmon Resonance at the WO_{3-x} Quantum Dot/Silver Nanowire Interface: SERS and Photocatalysis. *Nanoscale* **2019**, *11*, 5535–5547.
118. Dong, P.; Yang, B.; Liu, C.; et al. Highly Enhanced Photocatalytic Activity of WO_3 Thin Films Loaded with Pt-Ag Bimetallic Alloy Nanoparticles. *RSC Adv.* **2017**, *7*, 947–956.
119. Hajiahmadi, Z.; Azar, Y.T. Computational Study of H-WO_3 Surfaces as a Semiconductor in Water-Splitting Application. *Surf. Interfaces* **2022**, *28*, 101695.

120. Muhammad, E.; Jan, T.; Jalil, A. Experimental and Computational Study of Bi_2O_3/WO_3 Heterostructures as Efficient Solar Driven Photocatalyst. *Inorg. Chem. Commun.* **2025**, *171*, 113581.
121. Diaby, M.; Alimi, A.; Bardaoui, A.; et al. Correlation between the Experimental and Theoretical Photoelectrochemical Response of a WO_3 Electrode for Efficient Water Splitting through the Implementation of an Artificial Neural Network. *Sustainability* **2023**, *15*, 11751.
122. Knöppel, J.; Kormányos, A.; Mayerhöfer, B.; et al. Photocorrosion of WO_3 Photoanodes in Different Electrolytes. *ACS Phys. Chem. Au* **2021**, *1*, 6–13.
123. Ho, H.H.; Zahran, Z.N.; Chandra, D.; et al. Highly Stable and Efficient Photoelectrochemical Water Oxidation at an Anisotropically Crystallized Monoclinic WO_3 Film with Predominant Growth of the (202) Plane. *J. Mater. Chem. A* **2025**, *13*, 17898–17909.
124. Speldrich, S.; Wark, M.; Wittstock, G. Metal Oxide Protection Layers for Enhanced Stability and Activity of WO_3 Photoanodes in Alkaline Media. *ACS Appl. Energy Mater.* **2023**, *6*, 9602–9614.
125. Jakubow-Piotrowska, K.; Kurzydlowski, D.; Wrobel, P.; et al. Photoelectrochemical Behavior of WO_3 in an Aqueous Methanesulfonic Acid Electrolyte. *ACS Phys. Chem. Au* **2022**, *2*, 299–304.
126. Zeng, Q.; Gao, Y.; Lyu, L.; et al. Highly Improved Photoelectrocatalytic Efficiency and Stability of WO_3 Photoanodes by the Facile in Situ Growth of TiO_2 Branch Overlayers. *Nanoscale* **2018**, *10*, 13393–13401.
127. Tam, B.; Pike, S.D.; Nelson, J.; et al. The Scalable Growth of High-Performance Nanostructured Heterojunction Photoanodes for Applications in Tandem Photoelectrochemical-Photovoltaic Solar Water Splitting Devices. *Chem. Sci.* **2025**, *16*, 7794–7810.
128. Cai, M.; Fan, P.; Long, J.; et al. Large-Scale Tunable 3D Self-Supporting WO_3 Micro-Nano Architectures as Direct Photoanodes for Efficient Photoelectrochemical Water Splitting. *ACS Appl. Mater. Interfaces* **2017**, *9*, 17856–17864.
129. Amer, M.S.; Arunachalam, P.; Ghanem, M.A.; et al. Photoelectrochemical Performance of Strontium Titanium Oxynitride Photo-Activated with Cobalt Phosphate Nanoparticles for Oxidation of Alkaline Water. *Nanomaterials* **2023**, *13*, 920.